

Readily Accessible Metallic Micro-Island Arrays for High-Performance Metal Oxide Thin-Film Transistors

Jaehyun Kim, Joon Bee Park, Ding Zheng, Joon-Seok Kim, Yuhua Cheng, Sung Kyu Park,* Wei Huang,* Tobin J. Marks,* and Antonio Facchetti*

Thin-film transistors using metal oxide semiconductors are essential in many unconventional electronic devices. Nevertheless, further advances will be necessary to broaden their technological appeal. Here, a new strategy is reported to achieve high-performance solution-processed metal oxide thin-film transistors (MOTFTs) by introducing a metallic micro-island array (M-MIA) on top of the MO back channel, where the MO is a-IGZO (amorphous indium-gallium-zinc-oxide). Here Al-MIAs are fabricated using honeycomb cinnamate cellulose films, created by a scalable breath-figure method, as a shadow mask. For IGZO TFTs, the electron mobility (μ_e) increases from $\approx 3.6 \text{ cm}^2 \text{ V}^{-1} \text{ s}^{-1}$ to near $15.6 \text{ cm}^2 \text{ V}^{-1} \text{ s}^{-1}$ for optimal Al-MIA dimension/coverage of $1.25 \text{ }\mu\text{m}/51\%$. The Al-MIA IGZO TFT performance is superior to that of controls using compact/planar Al layers (Al-PL TFTs) and Au-MIAs with the same channel coverage. Kelvin probe force microscopy and technology computer-aided design simulations reveal that charge transfer occurs between the Al and the IGZO channel which is optimized for specific Al-MIA dimensions/surface channel coverages. Furthermore, such Al-MIA IGZO TFTs with a high- k fluoride-doped alumina dielectric exhibit a maximum μ_e of $>50.2 \text{ cm}^2 \text{ V}^{-1} \text{ s}^{-1}$. This is the first demonstration of a micro-structured MO semiconductor heterojunction with submicrometer resolution metallic arrays for enhanced transistor performance and broad applicability to other devices.

mobility^[7–12] versus conventional amorphous silicon TFTs, as well as large area processability at low temperatures.^[13–16] Furthermore, MOTFTs are less affected by short channel effects.^[17–19] As in other transistor technologies, MOTFT performance strongly depends on the intrinsic semiconductor channel properties as well as the channel interfacial characteristics, including that of the top surface.^[20–22] Furthermore, MOTFTs are limited by uncontrollable back channel trap densities, restricting their application in high-resolution displays, as well as 3D and virtual reality devices.^[7,23–27]

Recently, several strategies were reported to enhance the performance of MOTFTs by adopting new device architectures, including dual gate implantation,^[28–30] high- k insulators,^[31–33] and semiconducting heterostructures.^[34–38] Among these strategies, low-dimensional bi- or multilayer heterostructures of different MOs have enhanced the carrier mobility and drive current in MOTFTs.^[39,40] These improvements typically originate from


confined free electrons within the potential well of the hetero-interface between two semiconductors having large Fermi energy differences.^[41] However, although these approaches are noteworthy, limitations in available component materials and control of leakage currents have compromised the fidelity of this platform.^[37,38] Another approach to enhance performance

1. Introduction

Metal oxide (MO) thin-film transistors (MOTFTs) have attracted considerable attention in both academia and industry because of attractions such as high optical transparency in the visible region,^[1–3] good air stability,^[4–6] and outstanding carrier

J. Kim, D. Zheng, W. Huang, T. J. Marks, A. Facchetti
Department of Chemistry and Materials Research Center
Northwestern University
2145 Sheridan Road, Evanston, IL 60208, USA
E-mail: t-marks@northwestern.edu; a-facchetti@northwestern.edu

J. B. Park, S. K. Park
Displays and Devices Research Lab. School of Electrical and Electronics
Engineering
Chung-Ang University
Seoul 06974, Korea
E-mail: skpark@cau.ac.kr

 The ORCID identification number(s) for the author(s) of this article can be found under <https://doi.org/10.1002/adma.202205871>.

© 2022 The Authors. Advanced Materials published by Wiley-VCH GmbH. This is an open access article under the terms of the Creative Commons Attribution License, which permits use, distribution and reproduction in any medium, provided the original work is properly cited.

J.-S. Kim
Department of Materials Science and Engineering
Northwestern University
2145 Sheridan Road, Evanston, IL 60208, USA

Y. Cheng, W. Huang
School of Automation Engineering
University of Electronic Science and Technology of China (UESTC)
Chengdu, Sichuan 611731, China
E-mail: whuang@uestc.edu.cn

A. Facchetti
Flexterra Corporation
8025 Lamon Avenue, Skokie, IL 60077, USA

DOI: 10.1002/adma.202205871

consists of depositing a metallic capping layer covering the entire TFT back channel.^[42–44] This approach can reduce the charge trap density in the semiconductor back channel, primarily originating from oxygen vacancies, which increase electron scattering and reduce carrier mobility.^[45–47] However, this approach suffers considerable issues since the enhanced field-effect mobility is accompanied by an increased off-current and more complex device manufacture.^[42,48] Furthermore, the development of unique (sub-)micrometer patterning fabrication methods for heterojunctions and other TFT architectures remain challenging.^[37]

Here, we report enhanced-performance amorphous indium-gallium-zinc-oxide (IGZO) TFTs by using aluminium micro-island arrays (Al-MIAs) defined on top of the IGZO back channel. Specifically, we explore Al-MIAs of varying dimensions/channel coverage fabricated by Al vapor deposition using diverse honeycomb cinnamate-cellulose (Cin-cell) films as shadow masks. The latter are fabricated using a simple solution breath figure process,^[49,50] thus avoiding high-cost e-beam lithography. Optimal Al-MIA dimension/coverage enhances IGZO TFT electron mobility from $3.64 \text{ cm}^2 \text{ V}^{-1} \text{ s}^{-1}$ (no Al-MIA) to $15.58 \text{ cm}^2 \text{ V}^{-1} \text{ s}^{-1}$ (51%/1.25 μm Al-MIA), along with low off-current and enhanced bias stress stability. Kelvin probe force microscopy (KPFM) measurements and technology computer-aided design simulations were carried out to explain these results and to clarify the underlying mechanism of enhanced mobility with low off-currents in Al-MIA devices. The results indicate that Al-MIA can uniformly transfer electrons to the IGZO and efficiently passivate surface trap sites of the IGZO back channel versus those having an identical coverage, but with compact Al layers covering the IGZO back channel. Finally, by utilizing a high-*k* fluoride-doped alumina

gate dielectric, Al-MIA-based IGZO TFTs exhibit a maximum field-effect mobility of $>50 \text{ cm}^2 \text{ V}^{-1} \text{ s}^{-1}$, demonstrating the great versatility of this strategy to enhance MOTFT charge transport.

2. Results and Discussion

A schematic of the fabrication process for IGZO Al-MIA TFTs is shown in **Figure 1a**. Honeycomb Cin-cell film masks, with apertures of ≈ 0.71 to $\approx 1.25 \mu\text{m}$ and thickness of $\approx 300 \text{ nm}$ (Figure 1b and Figure S1, Supporting Information), were fabricated with a modified breath figure method and lift off/transfer from a poly(vinyl alcohol) (PVA) sacrificial layer (see Experimental Section for more details).^[49,51,52] For TFT fabrication, IGZO films (In:Ga:Zn = 7:1:2 molar ratio, $\approx 20 \text{ nm}$ thick) were spin-coated onto n-doped Si/SiO₂ serving as gate contact/gate dielectric (300 nm thick) layers, respectively. The IGZO channel was patterned using conventional photolithography, and then 100 nm thick Al source/drain electrodes were thermally evaporated and patterned by a lift-off process (channel length = 50 μm , channel width = 100 μm). Finally, the Cin-cell mask was placed on the IGZO TFT array (see Figure S2, Supporting Information, for details) and Al (or Au as a counterexample) and was thermally evaporated to define the Al- (or Au-) MIAs ($\approx 40 \text{ nm}$ thick) on the IGZO TFT channel. The Al-MIA dimension varied from 0.71 ± 0.03 to $\approx 1.25 \pm 0.05 \mu\text{m}$, which corresponds to a variation of the channel area coverage with Al from 23% to 51%, respectively (Figure S3, Supporting Information). Remarkably, unlike conventional metal shadow masks that cannot be completely contacted to the sample, our Cin-cell film masks strongly adhere to the sample, and because of the nm thickness, identical dimensions between the mask size and

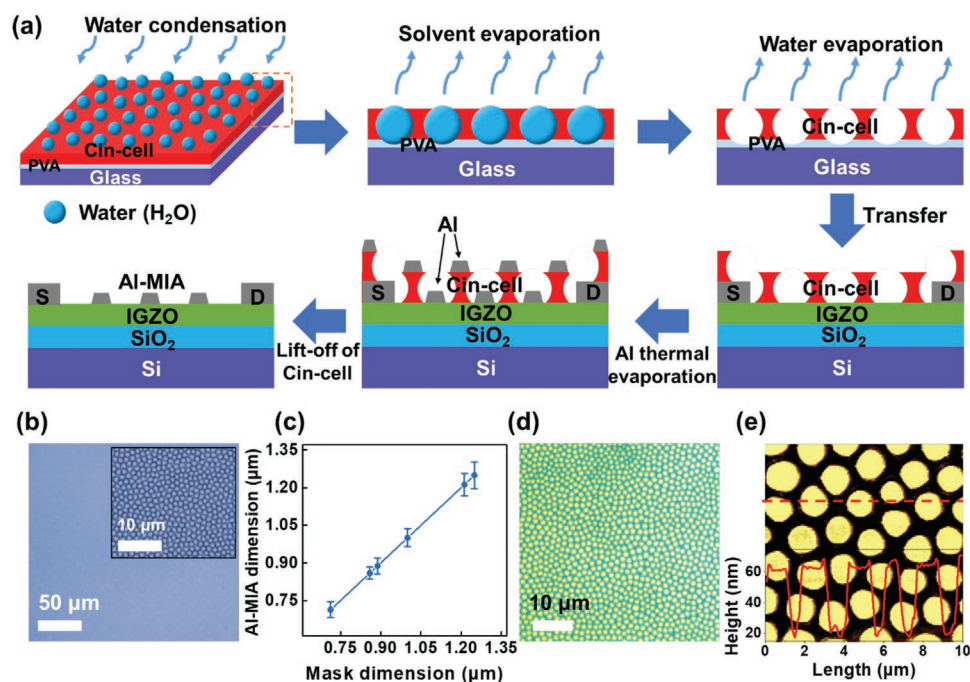


Figure 1. a) Schematic of the fabrication process for IGZO TFTs with Al-MIA. b) Optical microscopy images of a honeycomb Cin-cell film (inset figure is higher resolution) used as a shadow mask. c) Correlation between mask and Al-MIA dimensions. d) Optical microscopy image and e) AFM image with included the surface profile of an Al-MIA.

Al-MIA are obtained (Figure 1c). Figure 1d shows an optical image of an Al-MIA on IGZO demonstrating good large-area uniformity. Figure 1e and Figure S4 (Supporting Information) show AFM and SEM images of an Al-MIA on IGZO, respectively, employed for assessing MIA dimensions and thickness.

Next, the electrical performance of IGZO TFTs with Al-MIAs having different coverage/dimension was investigated. Furthermore, control IGZO TFTs having a planar and compact Al film (Al-PL) centered in the middle of the back channel and having different dimensions corresponding to a channel coverage from 20% to 60%, thus similar to those of MIAs, were also fabricated to assess the importance of a uniformly distributed versus compact channel coverage with Al (Figure S5, Supporting Information). Figure 2a,b and Figure S6 (Supporting Information) report representative transfer and output characteristics of the Al-MIA and Al-PL IGZO TFTs, respectively, and Table S1 (Supporting Information) summarizes all device performance parameters. Note, a large drain voltage ($V_D = +80$ V) was used to induce a high drain current because of the low SiO_2 film capacitance. In addition, Al source/drain electrodes were employed as ohmic contacts that lead to large saturation voltages. Both types of devices exhibit increased on-current (I_{on}) from 0.16 mA (no metal) to 0.76 and 0.63 mA when the Al coverage is increased to 51% for MIA and 60% for PL, respectively. However, while the off-current (I_{off}) of the Al-MIA IGZO TFTs remains very low (10^{-10} to 10^{-12} A) and comparable to that of the pristine IGZO TFTs, the I_{off} of the Al-PL IGZO TFTs increases dramatically to $>10^{-9}$ A when the Al coverage is $>50\%$. Thus, as shown in Figure 2c and Figure S7 (Supporting Information), the on/off current ratio (I_{on}/I_{off}) of the Al-MIA TFTs first slightly falls at low coverage (23%) but then gradually increases to 3.5×10^9 when the Al-MIA coverage reaches 51% due to the greater enhancement of the I_{on} ; however, that of the Al-PL

IGZO TFTs monotonically falls dramatically to 8.6×10^4 when the Al-PL coverage reaches 60%.

We also analyzed the I_{on}/I_{off} values of the Al-MIA and Al-PL IGZO TFTs with respect to the semiconductor channel thickness and the spacing between Al-MIAs (Figure S8, Supporting Information). As expected, both devices exhibit low I_{on}/I_{off} values as the channel thickness decreases from 35 to 7 nm because the high current density of the back channel becomes dominant. However, while the I_{on}/I_{off} of the Al-MIA IGZO TFTs slightly decreases from 5.97×10^9 to 1.63×10^8 when the channel thickness decreases from 35 to 7 nm, that of the Al-PL IGZO TFTs decreases to a greater extent from 3.42×10^8 to 2.35×10^5 . In addition, we find that the I_{on}/I_{off} of the Al-MIA IGZO TFTs only slightly decreases from 3.51×10^9 to 3.29×10^8 when the Al spacing between MIAs is increased from 0.55 to 0.81 μm . This result argues that the I_{on}/I_{off} values for Al-MIA IGZO TFTs are mainly dominated by the Al surface coverage, due to the efficient passivation of surface trap sites of the IGZO back channel.

The Al-MIA and Al-PL IGZO TFT figures of merit can be extracted in saturation from the equation,^[53] $\mu_{sat} = (2L/WC_{ox})(\delta I_D/\delta V_G)^2$, where μ_{sat} is the saturated field-effect mobility, L is the channel length, W is the channel width, C_{ox} is the gate insulator capacitance, I_D is the drain current (on-current) of the transistor, and V_G is the gate voltage. As shown in Figure 2d, both devices have enhanced μ_{sat} compared to that of the pristine IGZO TFTs ($\mu_{sat} = 3.64 \text{ cm}^2 \text{ V}^{-1} \text{ s}^{-1}$; see Figure S9, Supporting Information). However, while the μ_{sat} of the Al-MIA IGZO TFTs monotonically increases from $5.56 \text{ cm}^2 \text{ V}^{-1} \text{ s}^{-1}$ to $15.58 \text{ cm}^2 \text{ V}^{-1} \text{ s}^{-1}$ as the coverage increases from 23% to 51%, that of the Al-PL IGZO TFTs first increases from $5.28 \text{ cm}^2 \text{ V}^{-1} \text{ s}^{-1}$ (coverage = 20%) to $8.19 \text{ cm}^2 \text{ V}^{-1} \text{ s}^{-1}$ (coverage = 46%), but then falls to $7.16 \text{ cm}^2 \text{ V}^{-1} \text{ s}^{-1}$ when the coverage reaches 60%. This is attributed to saturation of the I_{on} and enhancement of the I_{off} , reducing the transconductance and thus the mobility of the Al-PL IGZO TFTs when the coverage is $>50\%$.^[42,48] Here, μ_{sat} of the best Al-MIA IGZO device is $>400\%$ and $>200\%$ that of the pristine IGZO and best Al-PL IGZO devices, respectively. Both the subthreshold slope (SS) and the threshold voltage (V_T) of IGZO TFTs with Al-MIA slightly increases from 0.16 to 0.20 V decade^{-1} and -7.38 to -9.90 V, respectively, as the Al-MIA coverage increases from 23% to 51%; however, those of the Al-PL devices dramatically increase from 0.16 to 0.77 V decade^{-1} and $+3.3$ to -20.0 V, respectively, as the coverage increases from 20% to 60% (Figure S10, Supporting Information). The slightly degraded SS value and negatively shifted V_T of both the Al-MIA and Al-PL IGZO TFTs, as the Al coverage increases, can be rationalized by the increased carrier density.^[48,54,55] Furthermore, since the SS change correlates with the total trap density (N_T) within the device channel region according to the equation $\Delta SS = qkTN_T t_{ch} \ln(10)/C_{ox}$,^[56] where q is the electron charge, k is Boltzmann's constant, T is the temperature, and t_{ch} is the channel thickness, the N_T of these devices can be extracted. It is found that N_T of the Al-MIA TFTs ($2.71 \times 10^{16} \text{ eV}^{-1} \text{ cm}^{-3}$) is far lower than that of the Al-PL TFTs ($3.64 \times 10^{17} \text{ eV}^{-1} \text{ cm}^{-3}$). In addition, we find that Al-PL IGZO TFTs exhibit a lower linear mobility (μ_{lin}) ($5.72 \text{ cm}^2 \text{ V}^{-1} \text{ s}^{-1}$) than μ_{sat} ($8.19 \text{ cm}^2 \text{ V}^{-1} \text{ s}^{-1}$), while Al-MIA IGZO TFTs exhibit similar μ_{lin} ($14.3 \text{ cm}^2 \text{ V}^{-1} \text{ s}^{-1}$) and μ_{sat} ($15.58 \text{ cm}^2 \text{ V}^{-1} \text{ s}^{-1}$) (Figure S11, Supporting Information),

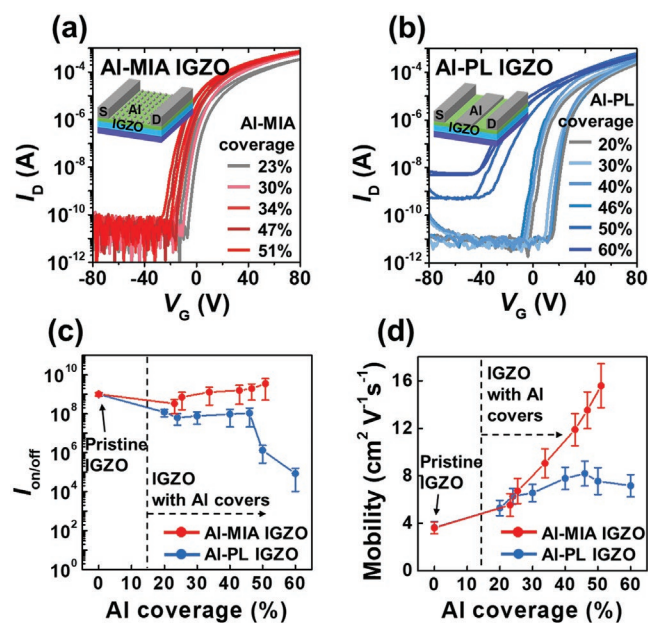


Figure 2. a) Representative transfer characteristics of IGZO TFTs with the indicated Al-MIA coverages. b) Representative transfer characteristics of IGZO TFTs with the indicated Al-PL coverages ($W/L = 100 \mu\text{m}/50 \mu\text{m}$, $V_D = 80$ V). c) I_{on}/I_{off} and d) μ_{sat} data for the indicated IGZO TFTs.

further supporting the assertion that the MIA coating minimizes charge trapping site.^[57,58] Finally, the operational stability under a positive bias stress for 3.6×10^3 s was monitored for the IGZO TFTs with optimal Al-MIA and PL coatings of 51% and 46%, respectively, and Figure S12 (Supporting Information) shows the corresponding transfer characteristics. The results indicate that the threshold voltage shift (ΔV_T) of the Al-MIA IGZO TFTs (+3.35 V) is far smaller than those of both the Al-PL (+18.35 V) and pristine IGZO (+19.1 V) TFTs. These data argue that the uniformly distributed Al-MIA is superior in passivating defect densities on the IGZO back-channel region.

In order to clarify the short channel effect such as drain induced barrier lowering (DIBL), we measured the change of the V_T of both Al-MIA and Al-PL IGZO TFTs on going from long ($L = 50 \mu\text{m}$) to short ($L = 5 \mu\text{m}$) channel lengths under various V_D measurement conditions. As shown in Figure S13 (Supporting Information), the Al-MIA IGZO TFTs exhibit negligible DIBL degradation at the short channel dimension, while Al-PL IGZO TFTs exhibit a large DIBL degradation. In addition, we tested the long-term stability of the Al-MIA IGZO TFTs. As shown in Figure S14 (Supporting Information), the Al-MIA IGZO TFTs show only a small variation of the $I_{\text{on}}/I_{\text{off}}$ and μ_{sat} (<5%) metrics even after 120 days of air exposure, while the Al-PL IGZO TFTs exhibit far larger degradations ($\approx 50\%$).

The most plausible reason for the variation of electron mobility is the change in back channel potential caused by the

difference in work function between the IGZO and the metallic capping layer.^[59,60] Figure S15 (Supporting Information) shows a schematic band structure representation of dielectric–semiconductor and dielectric–semiconductor–metal multilayers supporting, qualitatively, the mechanism underlying the observed performance variation between pristine and metal-covered IGZO TFTs. Thus, when the metal is Al (Figure 3a), electrons can be transferred from the low work function Al to the high work function IGZO layer, resulting in a positive potential in the IGZO.^[43] This positive potential promotes a down-shift of the IGZO band, increasing the electron density in the semiconductor. Thus, for an optimal Al structure and coverage (vide infra), the transferred electrons are sufficient to passivate traps and thereby increase I_{on} and μ_{sat} , but not large enough to create a back conducting channel increasing the I_{off} and deteriorating the $I_{\text{on}}/I_{\text{off}}$. This picture is further supported by an additional control experiment using gold (Au) as the metal of MIA (Au-MIA), which shows lower μ_{sat} and $I_{\text{on}}/I_{\text{off}}$ ratio, as well as a positively shifted V_T , versus both pristine and Al-MIA IGZO devices (Figure S16, Supporting Information). Indeed, the larger work function of Au versus IGZO would result in electron transfer from IGZO to Au, shift of the IGZO band up and depleting it of electrons (Figure 3b). To probe the reason underlying this result, X-ray photoelectron spectroscopy (XPS) measurements were carried out to determine the composition and the oxygen environment of pristine IGZO and

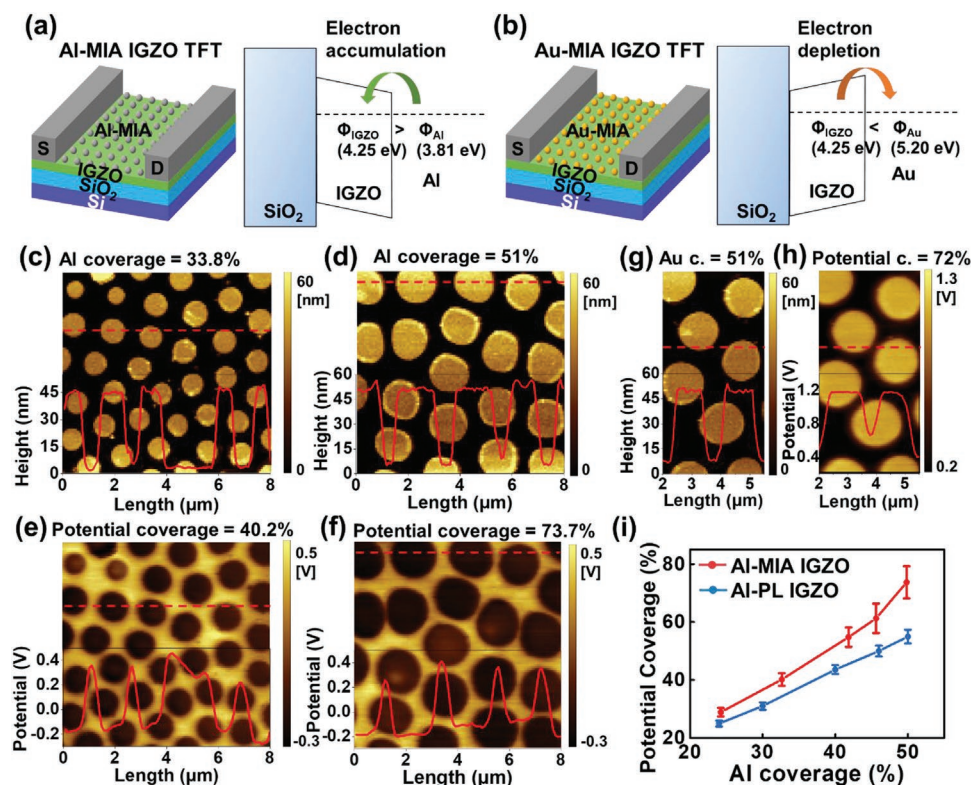


Figure 3. a,b) Schematic diagrams for device and band structure of Al-MIA IGZO TFTs (a) and Au-MIA IGZO TFTs (b). c–h) KPFM characterization of IGZO TFTs with Al (and Au)-MIA capping layers. c,d) AFM scan image and surface height profile along the cutline and e,f) corresponding surface potential mapping of IGZO TFTs with Al-MIA capping layers having different Al coverage. g) AFM scan image and surface height profile along the cutline and h) corresponding surface potential mapping of IGZO TFTs with Au-MIA capping layers. i) Potential coverage profile with respect to Al coverage of IGZO film with Al-MIA and Al-PL coatings.

Al-capped IGZO films (Figure S17, Supporting Information). Deconvolution of the O 1s spectra shows the contribution of peaks at 530.09 ± 0.01 , 531.21 ± 0.18 , and 532.19 ± 0.1 eV, corresponding to oxygen atoms in M–O–M lattice, oxygen atoms near oxygen vacancies (M–O_{vac}), and oxygen atoms in hydroxyl groups (M–OH compounds). Clearly, the M–O–M content of the Al-capped IGZO (72.5%) is larger than that of the pristine IGZO film (70.4%), while the M–OH content follows an opposite trend (7.2% vs 9.2%, respectively). This result indicates that the Al capping layer reduces the density of lattice defects.

Next, KPFM measurements were performed to map the IGZO surface potential with and without Al-MIA or Al-PL, which is acquired from the contact potential difference between an AFM probe and the surface of interest.^[61] Figure 3c–f as well as Figures S18 and S19 (Supporting Information) show the AFM topography and surface potential distribution maps of Al-MIA IGZO and Al-PL IGZO films. Independent Al architecture, the surface potential increases from ≈ -0.2 V on top of Al to $\approx +0.4$ V in the IGZO regions far from the metal in agreement with the work function difference between these two materials. Equally interesting is the comparison between topology and potential images that clearly show, on the contrary of the Al-PL, for the Al-MIA structure, the extent of the surface potential reduction covers a significant portion of the IGZO surface. Thus, while for an Al-PL structure, the topological and surface potential coverage almost coincide; for the Al-MIA structure having an Al coverage of ≈ 43 and $\approx 47\%$, the surface potential decrease extends to ≈ 55 and 61% , respectively (Figure 3i). This result demonstrates that MIA structures are more efficient in transferring/diffusing electrons to a larger portion of the IGZO back channel, when incorporated into a TFT, versus a PL architecture (Figure S20, Supporting Information). As expected, when using Au instead of Al-MIAs (Figure 3g,h), the surface potential on top of the metal (+1.3 V) is greater than in the IGZO (+0.4 V) and again the metal coverage is far smaller than the surface potential coverage, in line with efficient electron depletion of IGZO by Au-MIA.

Technology computer-aided design (TCAD) simulations of the band structure of pristine, Al-MIA, and Al-PL IGZO TFTs were next carried out to quantitatively analyze their transport behavior.^[62] These simulations incorporate the model experimental parameters from our devices, such as carrier mobility, bandgap, and permittivity^[63,64] to predict how changes in materials and device architecture affect charge-transport characteristics. The IGZO physical parameters used in the three device architectures are summarized in Table S2 (Supporting Information) and the simulated transfer characteristics of these IGZO TFTs are shown in Figure S21 (Supporting Information). Note that band alignment simulations were conducted by referring to the “affinity rule”, which assigns the conduction band discontinuity as equal to the difference between the electron affinities of the materials.^[65] Figure 4a,b shows the simulated energy band diagrams of an Al-capped IGZO TFT going from the top Al to the IGZO/SiO₂ interface in the on- ($V_G = +10$ V, $V_D = +10$ V) and off- ($V_G = -10$ V, $V_D = +10$ V) states, respectively. In both states potential wells form at the IGZO/Al heterointerface and their band energetics are little affected by V_G , suggesting that electrons will always accumulate in that region of the device back channel. Conversely, the energies of the

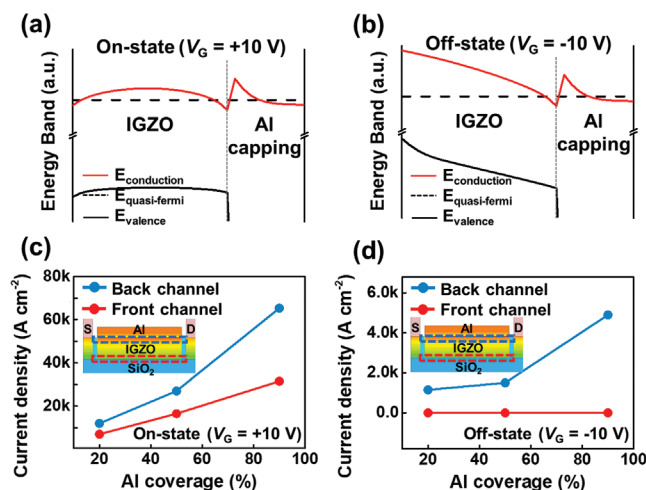


Figure 4. a,b) Simulated energy band diagrams with cutline from the Al layer to the IGZO/SiO₂ interface in the on-state ($V_G = 10$ V) (a) and off-state ($V_G = -10$ V) (b). c,d) Variation of the current densities of the back and front channel as a function of the Al coverage of IGZO TFTs with an Al layer in the on-state ($V_G = 10$ V) (c) and off-state ($V_G = -10$ V) (d).

on-/off-state bands moving to the dielectric surface, and thus the electron density (vide infra), are strongly modulated by the V_G , as expected by the field-effect. Next, to rationalize how the Al coverage affect the conductivity of these devices, the current densities originating from both the front and back channels in the on- (Figure 4c) and off- (Figure 4d) states of Al-PL devices as a function of Al coverage were simulated. For the devices in the on-state, the back and front channel current density increases from 12 to 65 kA cm^{-2} and from 7 to 31 kA cm^{-2} , respectively, with increasing the Al coverage from 20% to 90%. Thus, increasing the coverage is beneficial to enhance the on-current. However, simulations in the off-state indicate that while the current density of the front channel is always negligible (≈ 0.1 A cm^{-2}), the back channel current density first monotonically increases from 1.15 to 1.5 kA cm^{-2} as the Al coverage increases from 20% to 50%, but then exponentially to 4.9 kA cm^{-2} when the Al coverage increases to 90%. This result is in agreement with the strong reduction of the $I_{\text{on}}/I_{\text{off}}$ of the Al-PL devices when the Al coverage increases $>50\%$ (Figure S6, Supporting Information). Therefore, optimization of Al coverage and topology (vide infra) is essential for reducing the off-current of IGZO/Al heterostructures and optimizing device performance. Note that the TCAD simulations were conducted under low gate and drain bias conditions to avoid undesirable potential distortion issues near the drain electrode. Under higher gate bias conditions ($V_G = 80$ V), the current density of the front channel is far larger than that of the back channel due to the large electron concentration induced by the large positive gate potential (Figure S22, Supporting Information).

Furthermore, we also performed additional TCAD simulations to understand the enhanced charge transport in Al-MIA IGZO TFTs versus the other devices. Figure 5a–c shows the contour of electron concentrations (n) in the pristine, Al-PL, and Al-MIA IGZO TFTs in the on-state ($V_G = +10$ V, $V_D = +10$ V), respectively, with the latter two having the same Al coverage (50%). By monitoring the electron concentration

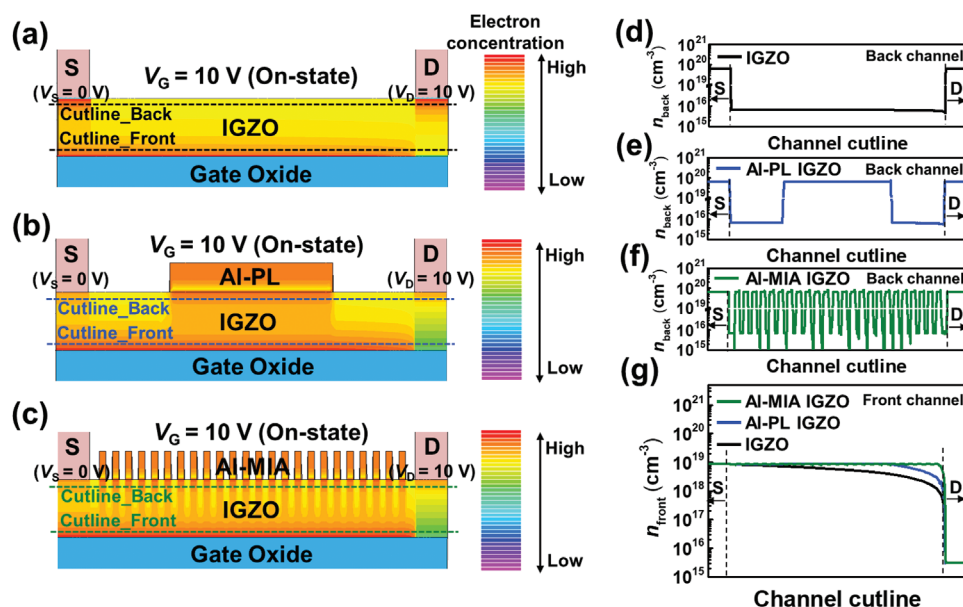


Figure 5. a–c) Contour of electron concentration in the IGZO TFTs, IGZO TFTs (a) with Al-PL (b) and Al-MIA (c) in the on-state ($V_G = 10$ V). d–g) Electron concentration profiles in IGZO TFTs (d) and IGZO TFTs with Al-PL (e) and Al-MIA (f) along the back channel cutline and along the front channel cutline (g).

of these devices in the back channel (n_{back} , see data from the cutlines of Figure 5a–c in Figure 5d–f, respectively), the n_{back} in the IGZO channel of the pristine device is low and very uniform (6.8×10^{15} cm $^{-3}$, Figure 5d) while that of the other devices is very large in the IGZO back channel region under the Al ($\approx 7 \times 10^{19}$ cm $^{-3}$, Figure 5e,f), in agreement with the considerable electron diffusion from Al to the IGZO channel. Furthermore, the large n_{back} in IGZO of Al-MIA ($>10^{19}$ cm $^{-3}$) exceeds the Al coverage and reaches $\approx 73\%$ of the back channel region, versus in IGZO with Al-PL only exhibits $\approx 52\%$, fully consistent with the KPFM analyses above. Importantly, analysis of the IGZO electron concentrations in the front channel (n_{front} , Figure 5g) indicates that the Al-MIA IGZO TFTs also exhibit an overall much higher average n_{front} (8.5×10^{18} cm $^{-3}$) than those of the pristine (5.3×10^{18} cm $^{-3}$) and Al-PL (7.5×10^{18} cm $^{-3}$) devices, because the uniform Al MIA distribution percolates carriers throughout the entire channel. This result suggests that the Al-MIA layer can enhance the conductivity of the entire IGZO channel region under the positive gate bias but, simultaneously, retain a low I_{off} . Furthermore, we carried out additional TCAD simulations to analyze the carrier concentrations of the Al-PL and Al-MIA IGZO TFTs at a higher drain bias ($V_D = 80$ V). As shown in Figure S23 (Supporting Information), in the on-state ($V_G = +80$ V, $V_D = +80$ V), the high drain bias simulations also show the enhanced electron concentrations for both back and front channels of the Al-MIA structure. In addition, we performed additional TCAD simulations to compute the electron concentration and current density of both Al-MIA and Al-PL IGZO TFTs in the off-state ($V_G = -80$ V, $V_D = +80$ V) as shown in Figure S24 (Supporting Information). The electron concentration in the IGZO back channel (n_{back}) of the pristine IGZO TFT gradually falls on going from the source (8.9×10^{14} cm $^{-3}$) to drain electrode (1.1×10^{12} cm $^{-3}$) and that of the Al-capped IGZO TFTs exhibits a uniform increased of electron concentration in

the region(s) under the Al layer. Thus, the Al-PL IGZO TFTs exhibit a large and uniform n_{back} under the Al-PL ($>10^{17}$ cm $^{-3}$), whereas effective modulation from high to low n_{back} is found for the Al-MIA. Thus, the oscillating carrier density throughout the back channel and the reduced n_{back} near the drain electrode region also suppress the off-current for the Al-MIA IGZO TFTs. Furthermore, the back channel current density of the Al-PL IGZO TFTs first monotonically increases from 0.82 to 1.07 kA cm $^{-2}$ as the Al coverage increases from 20% to 50%, but then dramatically increases to 2.57 kA cm $^{-2}$ when Al PL coverage increases to 90%. In contrast, the current density of the Al-MIA IGZO TFTs only increases from 0.27 to 0.92 kA cm $^{-2}$ as the coverage increases from 20% to 90%. Meanwhile, we measured electric field distribution for both Al-MIA and Al-PL IGZO TFTs as shown in Figure S25 (Supporting Information). The Al-MIA IGZO TFTs exhibit an overall much higher average electric field distribution in the back (E_{back}) and front channel (E_{front}) (8.2×10^6 and 1.9×10^7 V cm $^{-1}$, respectively) than the Al-PL devices (5.8×10^6 and 1.1×10^7 V cm $^{-1}$, respectively). This stronger electric field of the Al-MIA devices is expected to enhance electron accumulation in the channel. Note, we also simulated the electron concentrations of the IGZO layer for Au-MIA devices (Figure S26, Supporting Information), demonstrating that n_{back} in the IGZO channel under the Au (≈ 16.8 cm $^{-3}$) is far lower than that of pristine IGZO channel, again a result fully consistent with experiment.

Finally, we employed a high-quality low-temperature solution-processed fluoride-doped alumina (F:AlO $_x$) gate dielectric to further demonstrate the attraction of Al-MIA IGZO TFTs. This laboratory recently reported that F:AlO $_x$ gate insulator films show enhanced capacitance stability over a broad frequency range by suppressing polarization mechanisms at low frequencies, leading to stable and durable high- κ AlO $_x$ dielectrics.^[6] The device structure (Figure S27, Supporting Information) con-

sists of a n-doped Si gate, a ≈ 20 nm thick F:AlO_x dielectric layer (C_{ox} of 306 nF cm⁻², Figure S28, Supporting Information), an IGZO channel, Al source-drain contacts, and completed with an Al-MIA having the optimal coverage of $\approx 51\%$. The cut-off frequency was calculated from the equation, $f_T = g_m/2\pi C_g$ where f_T is the cut-off frequency, g_m is the transconductance, and C_g is the total gate capacitance. The Al-MIA IGZO TFTs exhibit increased f_T from to 626 kHz (no capping) to 1.12 MHz in spite of increased parasitic capacitance overlap, due to the greatly increased mobility. Representative transfer and output characteristics are shown in Figure S27b,c (Supporting Information), respectively, with the performance statistics collected in Figure S27d–f (Supporting Information). These devices operate within 2 V and exhibits μ_{sat} as high as 50.25 cm² V⁻¹ s⁻¹.

3. Conclusions

An effective and scalable strategy is presented to fabricate high-performance MOTFTs using M-MIA capping of the IGZO semiconductor channel. Using Al as the metal and a MIA with an optimized dimension/coverage of 1.25 $\mu\text{m}/\approx 50\%$, an optimal and uniform electron density is obtained in the IGZO back channel, minimizing charge trapping, enhancing electron transport, but retaining a low off-current. Importantly, the (sub-)micrometer Al-MIA structures are easily fabricated using inexpensive solution-processed honeycomb Cin-cell masks, which should greatly lower manufacturing costs versus conventional (sub-)micrometer lithographic processes. The efficient charge transport in Al-MIA devices, versus pristine and Al-PL IGZO TFTs, was explained by experimental KPFM measurements and TCAD simulations. Furthermore, a high mobility of >50.25 cm² V⁻¹ s⁻¹ was demonstrated in Al-MIA IGZO TFTs combining an optimized structure and a low-temperature solution-processed fluoride-doped alumina gate dielectric. The results reported here provide a new avenue to utilize conventional electronic materials to achieve high performance semiconductor devices, offering compatibility with commercial large-area and low-cost device applications, and open the door to the utilization of new materials for applications in other devices and field of use requiring easily accessible (sub-)micrometer architectures.

4. Experimental Section

Preparation of Precursor Solutions: For the IGZO precursor solution, each metal nitrate salt (354.8 mg of In(NO₃)₃·xH₂O, 399.6 mg of Ga(NO₃)₃·xH₂O, and 297.2 mg of Zn(NO₃)₂·xH₂O, all from Sigma-Aldrich, 99.999% pure) was dissolved in 10 mL deionized water and the precursor solutions were stirred for ≈ 1 h. Next, the precursor solutions were combined to the desired molar ratio (In:Ga:Zn = 7:1:2) and stirred before deposition by spin-coating. For the fluoride-doped AlO_x (F:AlO_x) precursor solution, 93.78 mg of Al(NO₃)₃ was dissolved in 5 mL of 2-methoxyethanol (2-ME) (anhydrous, Sigma Aldrich). Next, 25 μL of acetylacetone (AcAc) and 11.25 μL of 14.5 M NH₃(aq) were added and the solution was stirred overnight (>10 h). Finally, 25 wt% of 1,1,1-trifluoro-2,4-pentanediol (Sigma Aldrich) was added and the solution was stirred 1 h before spin-coating. The Cin-cell polymer was synthesized according to Ref. [67] and was dissolved in chloroform (16 mg mL⁻¹ concentration) and the solution was stirred >8 h before use. The Cin-cell solution was mixed with methanol (Sigma-Aldrich) with a volume ratio from 5 to 12.5% to afford the honeycomb film pore size from 0.71 to ≈ 1.25 μm .^[50,68]

Thin-Film Transistor Fabrication: All solutions were filtered through 0.2 μm PFET syringe filters before deposition. For the fabrication of the devices on SiO₂, heavily doped (n⁺⁺) silicon wafers with a 300 nm thick thermally grown SiO₂ were used as the gate/dielectric substrate. The substrates were cleaned by ultrasonication in acetone and isopropyl alcohol (IPA) sequentially and then treated to an oxygen plasma for 20 min to eliminate any organic residues and to improve the wettability for solution coating. Next, the IGZO solution was spin-coated onto the substrate at 3000 rpm for 20 s and was annealed at 300 °C for 30 min. This process was repeated three times to obtain the desired IGZO film thickness and improve stability. The IGZO channel was patterned by conventional photolithography and wet etching. Finally, 100 nm of aluminium (Al) source and drain (S/D) electrodes were deposited by thermal evaporation and patterned by a lift-off process. For the fabrication of the devices on F:AlO_x gate dielectrics, the F:AlO_x precursor solution was spin-coated onto heavily doped (n⁺⁺) silicon substrates at 3500 rpm for 30 s in a controlled humidity box (relative humidity $<20\%$) and pre-annealed at 120 °C for 60 s, followed by annealing at 300 °C for 1 min. This process was repeated four times to obtain the optimal dielectric film thickness (≈ 20 nm). The IGZO film was fabricated as described previously for the devices with SiO₂. The channel was patterned by photolithography and wet etching and, finally, Al S/D electrodes were deposited by thermal evaporation and patterned by lift-off process. All channel width and length of these TFTs are 100 and 50 μm , respectively.

Metal Layer Fabrication: For the fabrication of Al-PL architectures, Al was deposited on the pristine IGZO devices by thermal evaporation and patterned by a lift-off process. For the fabrication of Al-MIA, a glass (0.13–0.17 mm thick) was used as a carrier substrate. Poly(vinyl alcohol) (87%–89% hydrolysed, Sigma Aldrich) solution (16 mg/mL in deionized water), which was filtered through a 0.45 μm Nylon filter, was spin-coated onto the carrier substrate and annealed at 110 °C for 1 min. Next, the Cin-cell precursor solution was spin-coated onto the PVA-coated carrier substrate at 5000 rpm for 10 s in a controlled humidity box (relative humidity $>92\%$). The honeycomb structure of Cin-cell was detached from the carrier substrate by water immersion and transferred to the IGZO TFTs. Finally, Al was deposited onto the IGZO TFTs by thermal evaporation and patterned by lift-off of the honeycomb Cin-cell film.

Film and Device Characterizations: All IGZO devices were characterized using an Agilent B1500A semiconductor parameter analyzer in ambient air at room temperature. In the saturation region, the drain current of TFTs can be expressed with the conventional metal-oxide-semiconductor field-effect transistor model by the following equation, $I_D = (W/2L)\mu_{sat}C_{ox}(V_G - V_T)^2$. Then the μ_{sat} was extracted by $\mu_{sat} = (2L/WC_{ox})(\delta I_D/\delta V_G)^2$. In the linear region, drain current can be expressed by the following equation, $I_D = (W/L)\mu_{lin}C_{ox}(V_G - V_T)V_D$. Then, the μ_{lin} was extracted by $\mu_{lin} = (L/W)(1/C_{ox})(1/V_D)(\delta I_D/\delta V_G)$. The capacitor characteristics of F:AlO_x were measured using an Agilent 1500 semiconductor parameter analyzer or a Bio-Logic SP-150. Film morphologies were accessed using optical microscopy (ECLIPSE E200LED MV, Nikon), SEM (S-4800, Hitachi), and AFM (Dimension Icon Atomic Force Microscope, Bruker). The surface potentials were measured using KPFM (PeakForce AFM, Bruker), where the Pt/Ir-coated conductive tips (NanoAndMore PPP-EFM) were lifted 50–70 nm from the sample surface. The work function values of the metals and IGZO were clarified according to Ref. [43] and by KPFM measurements. The optical absorption spectra were measured with a Varian Cary 100 Bio UV–vis Spectrophotometer.

IGZO Characterization Dataset for TCAD Simulations: To analyze the conducting behaviors of the devices, TCAD simulations were carried out using the Silvaco ATHENA 2D device simulator.^[62] For the simulation profile, the physical parameters of IGZO devices, such as bandgap, mobility, and permittivity,^[63,64] were extracted from the measured I_D – V_G characteristics and our previous results.^[37] Table S2 (Supporting Information) summarizes all the data. To fit the simulation data with the device experimental results, a distinct subgap density of state (DOS) parameters was tuned, which were acceptor state and donor state. The subgap DOS parameters are described as superposition of tail and deep

states, following the exponential decay model and Gaussian distribution model equations:^[69]

$$N_{\text{Tail-acceptor}}(E) = N_{\text{TA}} \exp\left[(-E_C - E)/W_{\text{TA}}\right] \quad (1)$$

$$N_{\text{deep-acceptor}}(E) = N_{\text{GA}} \exp\left[(-E - E_{\text{GA}})/W_{\text{GA}}^2\right] \quad (2)$$

$$N_{\text{Tail-donor}}(E) = N_{\text{TD}} \exp\left[(-E_V - E)/W_{\text{TD}}\right] \quad (3)$$

$$N_{\text{deep-donor}}(E) = N_{\text{GD}} \exp\left[(-E - E_{\text{GD}})/W_{\text{GD}}^2\right] \quad (4)$$

where E_C is the conduction band energy, E_V is the valence band energy, N_{TA} is the intensity of states of acceptor-like tail states, N_{TD} is the intensity of states of donor-like tail states, N_{GA} is the intensity of states of acceptor-like deep states, and N_{GD} is the intensity of states of donor-like deep states. W_{TA} and W_{TD} are decay constants of tail states and W_{GA} and W_{GD} are full width half maximum of deep states. E_{GA} and E_{GD} are mean energy level of deep states. Since the E_{GD} values have not been exactly known yet, E_{GD} was assumed as the "Alessandro energy level of the bandgap."^[69]

Supporting Information

Supporting Information is available from the Wiley Online Library or from the author.

Acknowledgements

The authors thank AFOSR (FA9550-18-1-0320), the Northwestern U. MRSEC (NSF DMR-1720139), and Flexterra Inc. for support of this research. This work made use of the J. B. Cohen X-Ray Diffraction Facility, EPIC facility, Keck-II facility, and SPID facility of the NUANCE Center at Northwestern U., which received support from the Soft and Hybrid Nanotechnology Experimental (SHyNE) Resource (NSF NNCI-1542205), the MRSEC program (NSF DMR-1720139) at the Materials Research Center, the International Institute for Nanotechnology (IIN), and the Keck Foundation; and the State of Illinois, through the IIN.

Conflict of Interest

The authors declare no conflict of interest.

Author Contributions

J.K., D.Z., S.K.P., W.H., T.J.M., and A.F. conceived and designed the experiments. J.K., D.Z., and J.-S.K. performed the experiments of thin-film transistors. J.K. and J.B.P. performed the TCAD simulation. J.B.P., D.Z., Y.C., and W.H. helped analyze the data. J.K., S.K.P., W.H., T.J.M., and A.F. wrote the paper.

Data Availability Statement

The data that support the findings of this study are available in the supplementary material of this article.

Keywords

amorphous indium-gallium-zinc-oxide, metallic capping layers, metal oxide semiconductors, technology computer-aided design simulations, thin-film transistors

Received: June 28, 2022

Revised: August 15, 2022

Published online: October 11, 2022

- [1] M. N. Le, K. J. Baeg, K. T. Kim, S. H. Kang, B. D. Choi, C. Y. Park, S. P. Jeon, S. Lee, J. W. Jo, S. Kim, J. G. Park, D. Ho, J. Hong, M. Kim, H. K. Kim, C. Kim, K. Kim, Y. H. Kim, S. K. Park, M. G. Kim, *Adv. Funct. Mater.* **2021**, *31*, 2103285.
- [2] S. K. Sarkar, D. Maji, J. A. Khan, S. Kurup, D. Gupta, *ACS Appl. Electron. Mater.* **2022**, *4*, 2442.
- [3] K. Banger, C. Warwick, J. Lang, K. Broch, J. E. Halpert, J. Socratous, A. Brown, T. Leedham, H. Sirringhaus, *Chem. Sci.* **2016**, *7*, 6337.
- [4] D. Li, J. Du, Y. Tang, K. Liang, Y. Wang, H. Ren, R. Wang, L. Meng, B. Zhu, Y. Li, *Adv. Funct. Mater.* **2021**, *31*, 2105887.
- [5] J.-W. Jo, J. Kim, K.-T. Kim, J.-G. Kang, M.-G. Kim, K.-H. Kim, H. Ko, Y.-H. Kim, S. K. Park, *Adv. Mater.* **2015**, *27*, 1182.
- [6] S. H. Kang, I. S. Lee, K. Kwak, K. T. Min, N. B. Choi, H. W. Hwang, H. C. Choi, H. J. Kim, *ACS Appl. Electron. Mater.* **2022**, *4*, 2372.
- [7] L. Lu, J. Li, H. S. Kwok, M. Wong, *2016 IEEE Int. Electron Devices Meeting (IEDM)*, IEEE, Piscataway, NJ, USA **2016**, <https://doi.org/10.1109/IEDM.2016.7838526>.
- [8] K. Nomura, H. Ohta, A. Takagi, T. Kamiya, M. Hirano, H. Hosono, *Nature* **2004**, *432*, 488.
- [9] C. Chen, B. R. Yang, G. Li, H. Zhou, B. Huang, Q. Wu, R. Zhan, Y. Y. Noh, T. Minari, S. Zhang, S. Deng, H. Sirringhaus, C. Liu, *Adv. Sci.* **2019**, *6*, 1801189.
- [10] V. Pecunia, K. Banger, H. Sirringhaus, *Adv. Electron. Mater.* **2015**, *1*, 1400024.
- [11] J. T. Li, H. L. Tsai, W. Y. Lai, W. S. Hwang, I. G. Chen, J. S. Chen, *Appl. Phys. Lett.* **2018**, *112*, 183502.
- [12] Y. Zhao, Z. Wang, G. Xu, L. Cai, T. H. Han, A. Zhang, Q. Wu, R. Wang, T. Huang, P. Cheng, S. Y. Chang, D. Bao, Z. Zhao, M. Wang, Y. Huang, Y. Yang, *Adv. Funct. Mater.* **2020**, *30*, 2003285.
- [13] J. W. Park, B. H. Kang, H. J. Kim, *Adv. Funct. Mater.* **2020**, *30*, 1904632.
- [14] M.-G. Kim, M. G. Kanatzidis, A. Facchetti, T. J. Marks, *Nat. Mater.* **2011**, *10*, 382.
- [15] Y.-H. Kim, J.-S. Heo, T.-H. Kim, S. Park, M.-H. Yoon, J. Kim, M. S. Oh, G.-R. Yi, Y.-Y. Noh, S. K. Park, *Nature* **2012**, *489*, 128.
- [16] J. Socratous, K. K. Banger, Y. Vaynzof, A. Sadhanala, A. D. Brown, A. Sepe, U. Steiner, H. Sirringhaus, *Adv. Funct. Mater.* **2015**, *25*, 1873.
- [17] C. I. Yang, T. C. Chang, P. Y. Liao, L. H. Chen, B. W. Chen, W. C. Chou, G. F. Chen, S. C. Lin, C. Y. Yeh, C. M. Tsai, M. C. Yu, S. Zhang, *J. Electron. Devices Soc.* **2018**, *6*, 685.
- [18] Z. Wang, L. Luo, Y. Wang, J. Zhang, A. Song, *IEEE Trans. Electron Devices* **2022**, *69*, 561.
- [19] C. Sung, S. Nam, S. H. Cho, *IEEE Electron Device Lett.* **2021**, *42*, 1327.
- [20] J. Li, Y. Zhang, J. Wang, H. Yang, X. Zhou, M. Chan, X. Wang, L. Lu, S. Zhang, *IEEE Electron Device Lett.* **2022**, *43*, 729.
- [21] Y. S. Shiah, K. Sim, Y. Shi, K. Abe, S. Ueda, M. Sasase, J. Kim, H. Hosono, *Nat. Electron.* **2021**, *4*, 800.
- [22] Y. G. Park, D. Y. Cho, R. Kim, K. H. Kim, J. W. Lee, D. H. Lee, S. I. Jeong, N. R. Ahn, W. G. Lee, J. B. Choi, M. J. Kim, D. Kim, S. Jin, D. G. Park, J. Kim, S. Choi, S. Bang, J. W. Lee, *Adv. Electron. Mater.* **2022**, 2101273.
- [23] D. Striakhilev, B.-k. Park, S. J. Tang, *MRS Bull.* **2021**, *46*, 1063.
- [24] Y. Kang, W. Lee, J. Kim, K. Keum, S. H. Kang, J. W. Jo, S. K. Park, Y. H. Kim, *Mater. Res. Bull.* **2021**, *139*, 111252.
- [25] H. J. Jang, J. Y. Lee, J. Kwak, D. Lee, J. H. Park, B. Lee, Y. Y. Noh, *J. Inf. Disp.* **2019**, *20*, 1.
- [26] S. E. Ahn, I. Song, S. Jeon, Y. W. Jeon, Y. Kim, C. Kim, B. Ryu, J. H. Lee, A. Nathan, S. Lee, G. T. Kim, U. I. Chung, *Adv. Mater.* **2012**, *24*, 2631.
- [27] V. Pecunia, M. Nikolka, A. Sou, I. Nasrallah, A. Y. Amin, I. McCulloch, H. Sirringhaus, *Adv. Mater.* **2017**, *29*, 1606938.
- [28] C. Zhang, D. Li, P. T. Lai, X. D. Huang, *IEEE Electron Device Lett.* **2021**, *42*, 1176.

- [29] D. Bhatt, N. Kumar, S. Panda, *ACS Appl. Electron. Mater.* **2019**, *1*, 1465.
- [30] A. H. T. Nguyen, M. C. Nguyen, S. Cho, A. D. Nguyen, H. Kim, Y. Seok, J. Yoon, R. Choi, *Nano Converg* **2020**, *7*, 31.
- [31] A. Liu, H. Zhu, H. Sun, Y. Xu, Y. Y. Noh, *Adv. Mater.* **2018**, *30*, 1706364.
- [32] E. Carlos, J. Leppänen, A. Sneck, A. Alastalo, J. Deuermeier, R. Branquinho, R. Martins, E. Fortunato, *Adv. Electron. Mater.* **2020**, *6*, 1901071.
- [33] M. M. Islam, J. K. Saha, M. M. Hasan, J. Kim, R. N. Bukke, A. Ali, J. Jang, *Adv. Mater. Interfaces* **2021**, *8*, 2100600.
- [34] Y. S. Rim, H. Chen, X. Kou, H. S. Duan, H. Zhou, M. Cai, H. J. Kim, Y. Yang, *Adv. Mater.* **2014**, *26*, 4273.
- [35] M. H. Cho, C. H. Choi, J. K. Jeong, *ACS Appl. Mater. Interfaces* **2022**, *14*, 18646.
- [36] D. Khim, Y. H. Lin, T. D. Anthopoulos, *Adv. Funct. Mater.* **2019**, *29*, 1902591.
- [37] M. Lee, J. W. Jo, Y. J. Kim, S. Choi, S. M. Kwon, S. P. Jeon, A. Facchetti, Y. H. Kim, S. K. Park, *Adv. Mater.* **2018**, *30*, 1804120.
- [38] Y. Chen, W. Huang, V. K. Sangwan, B. Wang, L. Zeng, G. Wang, Y. Huang, Z. Lu, M. J. Bedzyk, M. C. Hersam, T. J. Marks, A. Facchetti, *Adv. Mater.* **2019**, *31*, 1805082.
- [39] H. J. Seul, J. H. Cho, J. S. Hur, M. H. Cho, M. H. Cho, M. T. Ryu, J. K. Jeong, *J. Alloys Compd.* **2022**, *903*, 163876.
- [40] S. Sanctis, J. Krausmann, C. Guhl, J. J. Schneider, *J. Mater. Chem. C* **2018**, *6*, 464.
- [41] Y. H. Lin, W. Li, H. Faber, A. Seitkhan, N. A. Hastas, D. Khim, Q. Zhang, X. Zhang, N. Pliatsikas, L. Tsetseris, P. A. Patsalas, D. D. C. Bradley, W. Huang, T. D. Anthopoulos, *Nat. Electron.* **2019**, *2*, 587.
- [42] H. W. Zan, C. C. Yeh, H. F. Meng, C. C. Tsai, L. H. Chen, *Adv. Mater.* **2012**, *24*, 3509.
- [43] K. T. Kim, J. Kim, Y. Kim, S. K. Park, *IEEE Electron Device Lett.* **2014**, *35*, 850.
- [44] H. Ferhati, F. Djeflal, L. B. Drissi, *J. Sci. Adv. Mater. Devices* **2022**, *7*, 100414.
- [45] W. K. Min, S. P. Park, H. J. Kim, J. H. Lee, K. Park, D. Kim, K. W. Kim, H. J. Kim, *ACS Appl. Mater. Interfaces* **2020**, *12*, 24929.
- [46] J. M. Park, H. Do Kim, H. Joh, S. C. Jang, K. Park, Y. C. Park, H. H. Nahm, Y. H. Kim, S. Jeon, H. S. Kim, *NPG Asia Mater* **2020**, *12*, 81.
- [47] S. H. Lee, S. Lee, S. C. Jang, N. On, H. S. Kim, J. K. Jeong, *J. Alloys Compd.* **2021**, *862*, 158009.
- [48] H. S. Cha, H. S. Jeong, S. H. Hwang, D. H. Lee, H. I. Kwon, *Electronics* **2020**, *9*, 2196.
- [49] X. Zhang, B. Wang, L. Huang, W. Huang, Z. Wang, W. Zhu, Y. Chen, Y. L. Mao, A. Facchetti, T. J. Marks, *Sci. Adv.* **2020**, *6*, eaaz1042.
- [50] A. Zhang, H. Bai, L. Li, *Chem. Rev.* **2015**, *115*, 9801.
- [51] L. S. Wan, L. W. Zhu, Y. Ou, Z. K. Xu, *Chem. Commun.* **2014**, *50*, 4024.
- [52] H. Yabu, K. Nagamine, J. Kamei, Y. Saito, T. Okabe, T. Shimazaki, M. Nishizawa, *RSC Adv.* **2015**, *5*, 88414.
- [53] H. W. Kim, E. S. Kim, J. S. Park, J. H. Lim, B. S. Kim, *Appl. Phys. Lett.* **2018**, *113*, 022104.
- [54] D. Wang, W. Zhao, H. Li, M. Furuta, *Materials (Basel)* **2018**, *11*, 559.
- [55] C. H. Woo, Y. Y. Kim, B. H. Kong, H. K. Cho, *Surf. Coatings Technol.* **2010**, *205*, S168.
- [56] K. W. Jo, W. J. Cho, *Appl. Phys. Lett.* **2014**, *105*, 213505.
- [57] D. S. Dolzhenkov, H. Zhang, J. Jang, J. S. Son, M. G. Panthani, T. Shibata, S. Chattopadhyay, D. V. Talapin, *Science* **2015**, *347*, 425.
- [58] S. M. Kwon, J. K. Won, J. Jo, J. Kim, H. Kim, H. Kwon, J. Kim, S. Ahn, Y. Kim, M. Lee, H. Lee, T. J. Marks, M. Kim, S. K. Park, *Sci. Adv.* **2018**, *4*, eaap9104.
- [59] B. H. Lee, A. Sohn, S. Kim, S. Y. Lee, *Sci. Rep.* **2019**, *9*, 886.
- [60] M. G. Shin, K. H. Bae, H. S. Jeong, D. H. Kim, H. S. Cha, H. I. Kwon, *Micromachines* **2020**, *11*, 917.
- [61] Z. Han, G. Xu, W. Wang, C. Lu, N. Lu, Z. Ji, L. Li, M. Liu, *Appl. Phys. Lett.* **2016**, *109*, 023509.
- [62] ATLAS Device Simul. Software Silvaco, St. Clara, CA, USA, **2014**.
- [63] T. C. Fung, C. S. Chuang, C. Chen, K. Abe, R. Cottle, M. Townsend, H. Kumomi, J. Kanicki, *J. Appl. Phys.* **2009**, *106*, 084511.
- [64] N. Preissler, O. Bierwagen, A. T. Ramu, J. S. Speck, *Phys. Rev. B – Condens. Matter Mater. Phys.* **2013**, *88*, 085305.
- [65] A. Klein, *Thin Solid Films* **2012**, *520*, 3721.
- [66] X. Zhuang, S. Patel, C. Zhang, B. Wang, Y. Chen, H. Liu, V. P. Dravid, J. Yu, Y. Y. Hu, W. Huang, A. Facchetti, T. J. Marks, *J. Am. Chem. Soc.* **2020**, *142*, 12440.
- [67] Z. Wang, X. Zhuang, Y. Chen, B. Wang, J. Yu, W. Huang, T. J. Marks, A. Facchetti, *Chem. Mater.* **2019**, *31*, 7608.
- [68] V. T. Bui, S. H. Ko, H. S. Choi, *ACS Appl. Mater. Interfaces* **2015**, *7*, 10541.
- [69] J. Jeong, Y. Hong, *IEEE Trans. Electron Devices* **2012**, *59*, 710.